Atmos. Chem. Phys. Discuss., https://doi.org/10.5194/acp-2018-276
Manuscript under review for journal Atmos. Chem. Phys.
Discussion started: 16 April 2018


Atmospheric Chemistry and Physics Discussions

# Analyzing the turbulence in the Planetary Boundary Layer by the synergic use of remote sensing systems: Doppler wind lidar and aerosol elastic lidar

Gregori de Arruda Moreira[1,2,3], Juan Luís Guerrero-Rascado[1,2], Jose Antonio Benavent-Oltra[1,2], Pablo Ortiz-Amezcua[1,2], Roberto Román[1,2,4], Andrés Esteban Bedoya-Velásquez[1,2,5] Juan Antonio Bravo-Aranda[1,2], Francisco Jose Olmo Reyes[1,2], Eduardo Landulfo[3], Lucas Alados-Arboledas[1,2]

[1]Andalusian Institute for Earth System Research (IISTA-CEAMA), Granada, Spain
[2]Dpt. Applied Physics, University of Granada, Granada, Spain
[3]Institute of Research and Nuclear Energy (IPEN), São Paulo, Brazil
[4]Grupo de Óptica Atmosférica (GOA), Universidad de Valladolid, Valladolid, Spain.
[5]Sciences Faculty, Department of Physics, Universidad Nacional de Colombia, Medellín, Colombia.

*Correspondence to*: Gregori de Arruda Moreira (gregori.moreira@usp.br)

**Abstract**

The Planetary Boundary Layer ($PBL$) is the lowermost region of troposphere and endowed with turbulent characteristics, which can have mechanical or thermodynamic origins. Such behavior gives to this layer great importance, mainly in studies about pollutant dispersion and weather forecasting. However, the instruments usually applied in studies about turbulence in the PBL have limitations in spatial resolution (anemometer towers) or temporal resolution (aircrafts). In this study we propose the synergetic use of remote sensing systems (microwave radiometer [$MWR$], Doppler lidar [$DL$] and elastic lidar [$EL$]) to analyze the $PBL$ behavior. Furthermore, we show how some meteorological variables such as air temperature, aerosol number density, vertical wind, relative humidity and net radiation might influence the $PBL$ dynamic. The statistical moments of the high frequency distributions of the vertical velocity, derived from $DL$ and of the backscattered coefficient derived from $EL$, are corrected by two methodologies, namely first lag and -2/3 correction. The corrected profiles present small differences when compare against the uncorrected profiles, showing low influence of noise and the viability of the proposed methodology. Two case studies were analyzed in detail, one corresponding to a well-defined $PBL$ and another one corresponding to a situation with presence of a Saharan dust lofted aerosol layer and clouds. In both cases the results provided by the different instruments are complementary, thus the synergistic use of the different systems allow us performing a detailed monitoring of the $PBL$.

**Keywords:** Turbulence, Planetary Boundary Layer, Doppler lidar, elastic lidar, microwave radiometer, Earlinet.

## 1 Introduction

The Planetary Boundary Layer ($PBL$) is the atmospheric layer directly influenced by the Earth's surface that responds to its changes within time scales around an hour (Stull, 1988). Such layer is located at the lowermost region of troposphere, and is mainly characterized by turbulent and cyclic process, which are responsible of its large variability along the day. In an ideal situation, instants after sunrise, ground surface temperature increase due to the positive net radiative flux ($R_n$). This process intensifies the convection and



enables the heating of the upper troposphere regions, originating the Convective Boundary Layer ($CBL$) or Mixing Layer ($ML$), which has this name due to a mixing process generated by this turbulent ascending air parcels. Some instants before sunset the gradual reduction of incoming solar irradiance at the Earth's surface causes the decrease of the positive $R_n$ and its change in sign. In this situation, there is a reduction of the convective processes and a weakening of the turbulence. In this process the $CBL$ leads to the development of two layers, namely a stably stratified boundary layer called Stable Boundary Layer ($SBL$) close to the surface, and the Residual Layer ($RL$) that contains features from the previous day's $ML$ and is just above the $SBL$.

Knowledge of the turbulent processes in the $CBL$ is important in diverse studies, mainly for atmospheric modeling and pollutant dispersion, since turbulent mixing can be considered as the primary process by which aerosol particles and other scalars are transported vertically in atmosphere. Because turbulent processes are treated as nondeterministic, they are characterized and described by their statistical properties (high order statistical moments). When applied to atmospheric studies such analysis provide information about the field of turbulent fluctuation, as well as, a description of the mixing process in the PBL (Pal et al., 2010).

Anemometer towers have been widely applied in studies about turbulence (e.g., Kaimal and Gaynor, 1983; van Ulden and Wieringa, 1996), however the limited vertical range of these equipment restrict the analysis to regions close to surface. Aircraft have also been used in atmospheric turbulence studies (e.g., Lenschow et al., 1980; Williams and Hacker, 1992; Lenschow et al., 1994; Albrecht et al., 1995; Stull et al., 1997; Andrews et al., 2004; Vogelmann et al., 2012), nevertheless their short time window limits the analysis. In this scenario, systems with high spatial and temporal resolution and enough range are necessary in order to provide more detailed results along the day throughout the whole thickness of the $PBL$.

In the last decades, lidar systems have been increasingly applied in this kind of study due to its large vertical range and high data acquisition rate. Several kind of tracers are used such as vertical wind velocity [Doppler lidar] (e.g. Lenschow et al., 2000; Lothon et al., 2006; O'Connor et al., 2010), water vapor [Raman lidar and DIAL] (e.g. Wulfmeyer, 1999; Kiemle et al., 2007; Wulfmeyer et al., 2010; Turner et al., 2014; Muppa et al., 2015), temperature [rotational Raman lidar] (e.g. Behrendt et al., 2015) and aerosol [elastic lidar] (e.g. Pal et al., 2010; McNicholas et al., 2015). This allows the observation of a wide range of atmospheric processes, especially when different lidar systems are synergistically applied, as for example Engelmann et al. (2008), who combined elastic and Doppler lidar data in order to identify the vertical particle flux.

In this study, we use synergistically the data of three remote sensing systems (Elastic Lidar [$EL$], Doppler Lidar [$DL$] and Microwave Radiometer [$MWR$]) acquired during the SLOPE-I campaign, held at IISTA-CEAMA (Andalusian Institute for Earth System Research, Granada, Spain) during May to August 2016, in order to analyze the PBL behavior and to improve our comprehension about how each analyzed variable influence the PBL dynamics.

This paper is organized as follows. Description of the experimental site and the equipment setup are presented in Section 2. The methodologies applied are introduced in Section 3. Section 4 presents the results of the analyses using the different methodologies. Finally, conclusions are summarized in Section 5.

Atmos. Chem. Phys. Discuss., https://doi.org/10.5194/acp-2018-276
Manuscript under review for journal Atmos. Chem. Phys.
Discussion started: 16 April 2018


Atmospheric Chemistry and Physics Discussions

## 2 Experimental site and Instrumentation

The SLOPE-I (Sierra nevada Lidar aerOsol Profiling Experiment) campaign was performed from May to September 2016 in South-Eastern Spain in the framework of the European Research Infrastructure for the observation of Aerosol, Clouds, and Trace gases (ACTRIS). The main objective of this campaign was to perform a closure study by comparing remote sensing system retrievals of atmospheric aerosol properties, using remote systems operating at the Andalusian Institute of Earth System Research (IISTA-CEAMA) and in-situ measurements operating at distinct altitudes in the Northern slope of Sierra Nevada, around 20 km away from IISTA-CEAMA (Bedoya-Velásquez et al., 2018; Román et al., 2018). The IISTA-CEAMA station is part of European Aerosol Research Lidar NETwork (EARLINET) (Pappalardo et al, 2014) since 2005 and at present is an ACTRIS station (http://actris2.nilu.no/). The research facilities are located at Granada, a medium size city in Southeastern Spain (Granada, 37.16°N, 3.61°W, 680 m a.s.l.), surrounded by mountains and with Mediterranean-continental climate conditions that are responsible of cool winters and hot summers. Rain is scarce, especially from late spring to early autumn. Granada is affected by different kind of aerosol particles locally originated and medium-long range transported from Europe, Africa and North America (Lyamani et al., 2006; Guerrero-Rascado et al., 2008, 2009; Titos et al., 2012; Navas-Guzmán et al., 2013; Valenzuela et al., 2014).

MULHACEN is a biaxial ground-based Raman lidar system operated at IISTA-CEAMA in the frame of EARLINET research network. This system operates with a pulsed Nd:YAG laser, frequency doubled and tripled by Potassium Dideuterium Phosphate crystals, emitting at wavelengths of 355, 532 and 1064 nm with output energies per pulse of 60, 65 and 110 mJ, respectively. MULHACEN operates with three elastic channels: 355, 532 (s and p) and 1064 nm and three Raman-shifted channels: 387 (from $N_2$), 408 (from $H_2O$) and 607 nm (from $N_2$) . MULHACEN's overlap is complete at 90% between 520 and 820 m a.g.l. for all the wavelengths, reaching full overlap around 1220 m a.g.l. (Navas-Guzmán et al ., 2011; Guerrero-Rascado et al. 2010). This system was operated with a temporal and spatial resolution of 2 s and 7.5 m, respectively. More details can be found at Guerrero-Rascado et al. (2008, 2009).

The Doppler lidar (Halo Photonics) model Stream Line is also operated at IISTA-CEAMA. This system works in continuous and automatic mode from May 2016. It operates at 1.5 µm with 300 gates. The range gate length is 30 m, with the first gate at 60 m. For this work the data were collected in Stare mode (laser beam is pointed at 90° with respect to the ground surface) with a time resolution of 2 s.

Furthermore, we operated the ground-based passive microwave radiometer (RPG-HATPRO G2, Radiometer Physics GmbH), which is part of the MWRnet [http://cetemps.aquila.infn.it/mwrnet/] (Rose et al., 2005 and Caumont et al., 2016). Since November 2011, this system operates in automatic and continuous mode at IISTA-CEAMA. The microwave radiometer (MWR) measures the sky brightness temperature with a radiometric resolution between 0.3 and 0.4 K root mean square error at 1 s integration time, using direct detection receivers within two bands, 22-31 GHz (water vapor - K band) and 51-58 GHz (oxygen - V band). From these bands is possible to obtain profiles of water vapor and temperature,



respectively, by inversion algorithms described in Rose et al. (2005). The range resolution of these profiles vary between 10 and 200 m in the first 2 km and between 200 and 1000 m in the layer between 2 and 10 km (Navas-Guzmán et al., 2014).

The meteorological sensor (HMP60, Vaisala) is used to acquire the air surface temperature and surface relative humidity, with a temporal resolution of 1 minute. Relative humidity is monitored with an accuracy of ± 3%, and air surface temperature is acquired with an accuracy and precision of 0.6º C and 0.01º C, respectively.

A CM-11 pyranometer manufactured by Kipp & Zonen (Delft, The Netherlands) is also installed in the ground-based station. This equipment measures the shortwave (SW) solar global horizontal irradiance data (305–2800 nm). The CM-11 pyranometer complies with the specifications for the first-class WMO (World Meteorological Organization) classification of this instrument (resolution better than ±5 $Wm^{-2}$), and the calibration factor stability has been periodically checked against a reference CM-11 pyranometer (Antón et. al, 2012).

## 3 Methodology

### 3.1 MWR data analyzes

The MWR data are analyzed combining two algorithms, Parcel Method $[PM]$ (Holzworth, 1964) and Temperature Gradient Method $[TGM]$ (Coen, 2014), in order to estimate the $PBLH$ ($PBLH_{MWR}$) in convective and stable situations, respectively. The different situations are discriminated by comparing the surface potential temperature ($\theta(z_0)$) with the corresponding vertical profile of $\theta(z)$ up to 5 km. Those cases where all the points in the vertical profile have values larger than $\theta(z_0)$ are labeled as stable, and $TGM$ is applied. Otherwise the situation is labeled as unstable and the $PM$ is applied. The vertical profile of $\theta(z)$ is obtained from the vertical profile of T(z) using the following equation (Stull, 2011):

$$\theta(z) = T(z) + 0.0098 * z \quad (1)$$

where $T(z)$ is the temperature profile provided by $MWR$, $z$ is the height above the sea level, and 0.0098 K/m is the dry adiabatic temperature gradient. A meteorological station co-located with the $MWR$ is used to detect the surface temperature $[T(z_0)]$. In order to reduce the noise, $\theta(z)$ profiles were averaged providing a $PBLH_{MWR}$ value at 30 minutes intervals.

### 3.2 Lidar turbulence analysis

Both lidar systems, $DL$ and $EL$, gathered data with a temporal resolution of 2 seconds. Then, the data are averaged in 1-hour packages, from which the mean value is extracted $[\bar{q}(z)]$. Such mean value is subtracted from each $q(z,t)$ profile in order to estimate the vertical profile of the fluctuation for the measured variable $[q'(z,t)]$ (i.e. vertical velocity for the $DL$):

Atmos. Chem. Phys. Discuss., https://doi.org/10.5194/acp-2018-276
Manuscript under review for journal Atmos. Chem. Phys.
Discussion started: 16 April 2018




$$q'(z,t) = q(z,t) - \bar{q}(z) \quad (2)$$

Then, from $q'(z,t)$ is possible to obtain the high-order moments (variance ($\boldsymbol{\sigma^2}$), skewness ($\boldsymbol{S}$) and kurtosis ($\boldsymbol{K}$)), as well as, the integral time scale ($\boldsymbol{\tau}$ - which is the time over which the turbulent process are highly correlated to itself) as shown in table 1. These variables can also be obtained from the following autocovariance function, $M_{ij}$:

$$M_{ij} = \int_0^{t_f} [q'(z,t)]^i [q'(z,t+t_f)]^j dt \quad (3)$$

where $t_f$ is the final time, $i$ and $j$ indicate the order of autocovariance function.

However, it is necessary to considerer that the acquired real data contain instrumental noise, $\varepsilon(z)$. Therefore, the equation 3 can be rewritten as:

$$M_{ij} = \int_0^{\tau} [q(z,t) + \varepsilon(z,t)]^i [q(z,t+\tau) + \varepsilon(z,t+\tau)]^j dt \quad (4)$$

The autocovariance function of a time series with zero lag results in the sum of the variances of the atmospheric variable and its $\varepsilon(z)$. Nevertheless, atmospheric fluctuations are correlated in time, but the $\varepsilon(z)$ is random and uncorrelated with the atmospheric signal. Consequently the noise is only associated with lag 0 (fig. 1). Based on this concept Lenschow et al. (2000) suggested to obtain the corrected autocovariance function, $M_{11}(\rightarrow 0)$, from two methods, namely first lag correction or -2/3 law correction. In the first method, $M_{11}(\rightarrow 0)$ is obtained directly by the subtraction of lag 0, $\Delta M_{11}(0)$, from the autocovariance function, $M_{11}(0)$. In the second method $M_{11}(\rightarrow 0)$ is generated by the extrapolation of $M_{11}(0)$ at firsts nonzero lags back to lag zero (-2/3 law correction). The extrapolation can be performed using the inertial subrange hypothesis, which is described by the following equation (Monin and Yaglom, 1979):

$$M_{11}(\rightarrow 0) = \overline{q'^2(z,t)} + Ct^{2/3} \quad (5)$$

where C represents a parameter of turbulent eddy dissipation rate. The high-order moments and $\boldsymbol{\tau}$ corrections and errors are shown in Table 1 (columns 2 and 3, respectively).

The same procedure of analysis is applied in studies with $DL$ and $EL$, being the main difference the tracer used by each system, which are the fluctuation of vertical wind speed ($w'$) for $DL$ and aerosol number density ($N'$) for $EL$. $DL$ provides $w(z,t)$ directly, and therefore the procedure described in Figure 2 can be applied directly. So, the two corrections described above are applied separately and finally $\boldsymbol{\tau}$ and high-order moments with and without corrections can be estimated.

On the other hand, the $EL$ does not provide $N(z,t)$ directly. Under some restrictions, it is possible to ignore the particle hygroscopic growth and to assume that the vertical distribution of aerosol type does not changes with time, and to adopt the following relation (Pal et al., 2010):

$$\beta_{par}(z,t) \approx N(z,t)Y(z) \Rightarrow \beta'_{par}(z,t) = N'(z,t) \quad (6)$$



where $\beta_{par}$ and $\beta'_{par}$ represent the particle backscatter coefficient and its fluctuation, respectively, and $Y$ does not depends on time.

Considering the lidar equation:

$$P_\lambda(z) = P_0 \frac{ct_d}{2} AO(z) \frac{\beta_\lambda(z)}{z^2} e^{-2\int_0^z \alpha_\lambda(z'dz')} \quad (7)$$

where $P_\lambda(z)$ is the signal returned from distance $z$ at time $t$, $z$ is the distance [m] from the lidar of the volume investigated in the atmosphere, $P_0$ is the power of the emitted laser pulse, $c$ is the light speed [m/s], $t_d$ is the duration of laser pulse [ns], $A$ is the area [m²] of telescope cross section, $O(z)$ is the overlap function, $\alpha_\lambda(z)$ is the total extinction coefficient (due to atmospheric particles and molecules) [(km)$^{-1}$] at distance $z$, $\beta_\lambda(z)$ is the total backscatter coefficient (due to atmospheric particles and molecules) [(km.sr)$^{-1}$] at distance $z$ and the subscribed $\lambda$ represents the wavelength. At 1064 nm, the two path transmittance term related to $\alpha(z)$ is considered as nearly negligible (Paul et al., 2010). Thus, it is possible to affirm that:

$$RCS_{1064}(z) = P(z)_{1064}.z^2 \cong G.\beta_{1064}(z) \quad (8)$$

and consequently:

$$RCS'_{1064}(z,t) \cong \beta'_{1064}(z,t) = \beta'_{par}(z,t) = N'(z,t) \quad (9)$$

where $RCS_{1064}$ and $RCS'_{1064}$ are the range corrected signal and its fluctuation, respectively, $G$ is a constant and the subscribed indexes represents the wavelength.

In this way, Pal et al. (2010) have shown the feasibility of using $EL$ operating at 1064 nm for describing the atmospheric turbulence. In a recent paper Moreira et al. (2018), have shown that the use of the $EL$ at 532 nm, in spite of the larger attenuation expected at this wavelength due to both aerosol and molecules, provides a description of the turbulence equivalent to that provided by $EL$ operating at 1064 nm. This result is interesting having in mind the more extended use of lidar systems based on laser emission at 532 nm in different coordinated networks. Thus, in EARLINET and LALINET around 76% and 45% of the systems include the wavelength of 1064 nm, while 95% of the EARLINET systems and 73% of the LALINET systems operate systems that include the wavelength 532 nm (Sicard et al., 2015; Guerrero-Rascado et al., 2016)). Furthermore, the performance of the lidar systems at 532 nm presents better signal to noise ratio than that encountered at 1064nm. Thus, in this study we use the $RCS_{532}$ for analyzing turbulence using $EL$, following the procedure described in Figure 3, which is basically the same methodology described earlier for $DL$.

## 4 Results

### 4.1 Error Analysis

The influence of random error in noisy observations rapidly grows for higher-order moments (i.e., the influence of random noise is much larger for the fourth-order moment than for the third-order moment).



Therefore, the first step, in order to ascertain the applied methodology and our data quality, we performed the error treatment of $DL$ data as described in Figure 2.

Figure 4 illustrate the autocovariance function, generates from $w'$, at three different heights. As mentioned before, the lag 0 is contaminated by noise $\varepsilon$, and thus the impact of the noise $\varepsilon$ increases with height, mainly above $PBLH_{MWR}$ (1100 m a.g.l. in our example).

Figure 5-A illustrates the comparison between integral time scale ($\boldsymbol{\tau_{w'}}$) without correction and the two corrections cited in section 3.2. Except for the first height, below the $PBLH_{MWR}$ the profiles practically do not have significant difference, as well as small errors bars. Above $PBLH_{MWR}$ the first lag correction presents some differences in relation the other profiles at around 1350 m.

Figures 5-B and 5-C show the comparison of variance ($\boldsymbol{\sigma^2_{w'}}$) and skewness ($\boldsymbol{S_{w'}}$), respectively, with and without corrections. Under the $PBLH_{MWR}$ the corrected vertical profiles do not present significant differences with the respective corrected profiles. Slight differences are evident above $PBLH_{MWR}$ when the first lag correction is applied.

For $EL$ we use the same procedure for the correction and error analysis that we apply to the DL data. Figure 6 shows the autocovariance function, obtained from $RCS'$, at three distinct heights. As expected, the increase of height produces the increase of $\varepsilon$, principally above the $PBLH_{MWR}$.

Figures 7-A, 7-B, 7-C and 7-D show the vertical profiles of $\boldsymbol{\tau_{RCS'}}$, $\boldsymbol{\sigma^2_{RCS'}}$, $\boldsymbol{S_{RCS'}}$ and kurtosis ($\boldsymbol{K_{RCS'}}$), respectively, with and without the corrections described in section 3.2. In general, the corrections do not affect the profiles in a significant way, especially in the region below the $PBLH_{MWR}$. Above the $PBLH_{MWR}$ some small differences are noticed, mainly in the first lag correction. The errors bars associated to each profile also have low values in all cases. When comparing corrected and uncorrected profiles, the largest differences are observed for the profiles at higher order moments, because of error propagation. $\boldsymbol{K_{RCS'}}$ profile is the more affected by corrections, so the kurtosis profile after the first lag correction shows the largest difference with uncorrected profile.

Since the first lag and 2/3 corrections do not have a significant impact within the PBL region, we adopted the first lag correction in order to be more careful during the comparison.

### 4.2 Case Studies

In this section we present two study cases, in order to show how the synergy of methodologies described in section 3 can provide a detailed description about $PBL$ behavior. The first case represents a typical day with a clear sky situation. The second case correspond to a more complex situation, where there is presence of clouds and Saharan mineral dust layers.

Atmos. Chem. Phys. Discuss., https://doi.org/10.5194/acp-2018-276
Manuscript under review for journal Atmos. Chem. Phys.
Discussion started: 16 April 2018




#### 4.2.1 Case Study I: clear sky situation.

In this case study we use measurements gathered with $DL$, $MWR$ and pyranometer during 24 hours. The $EL$ was operated under operator-supervised mode from 08:20 to 18:00 UTC.

Figure 8 (A) shows the integral time scale obtained from $DL$ data ($\boldsymbol{\tau_{w'}}$). The gray areas represents the region where $\boldsymbol{\tau_{w'}}$ is lower than the acquisition time of $DL$ and, therefore, for this region it is not possible to analyze turbulent processes. However, the gray area is located almost entirely above the $PBLH_{MWR}$ (white stars). Thus, the $DL$ acquisition time allows us to observe the turbulence throughout the whole $PBL$. The gray areas have the same meaning in Figures 8-B and 8-C.

$\boldsymbol{\sigma^2_{w'}}$ has low values during the entire period of $SBL$ (Figure 8-B). Nevertheless, as air temperature (black lines) begins to increase (around 07:00 UTC), $\boldsymbol{\sigma^2_{w'}}$ increases as well as, $PBLH_{MWR}$. $\boldsymbol{\sigma^2_{w'}}$ reaches its maximum values in the middle of the day, when we also observe the maximum values of air temperature and $PBLH_{MWR}$. This process is in agreement with the behavior of skewness of $w'$ ($\boldsymbol{S_{w'}}$) shown in Figure 8-C. $\boldsymbol{S_{w'}}$ is directly associated with the direction of turbulent movements. Thus, positive values correspond with surface heating while negative values are associated to cloud-top cooling. If $\boldsymbol{S_{w'}}$ is positive, both $\boldsymbol{\sigma^2_{w'}}$ and $TKE$ (Turbulent Kinetic Energy) are being transported upwards, consequently the red regions in Figure 13-C represents positive values of $\boldsymbol{S_{w'}}$ and the blue regions means negative ones. During the stable period, there is predominance of low values of $\boldsymbol{S_{w'}}$, nevertheless as air temperature increases, $\boldsymbol{S_{w'}}$ values begin to become positive and increase with the ascent of the $PBLH_{MWR}$. The $PBLH_{MWR}$ ascension follows the high convection regions. Around 18:00 UTC, air temperature begins to decrease, causing the reduction of $\boldsymbol{S_{w'}}$ and consequently of $PBLH_{MWR}$.

Figure 8-D shows the values of $R_n$ that are estimated from solar global irradiance values using the seasonal model described in Alados et al. (2003). The negative values of $R_n$ are concentrated in the stable region. Around 06:00 UTC, $R_n$ value begins to increase and reach its maximum in the middle of the day. Comparing figures 8-C and D, we can observe a similarity among the behavior of $\boldsymbol{S_{w'}}$, $R_n$ and surface air temperature, because these variable increase and decrease together, as expected. The increase of $R_n$ causes the increase of surface air temperature generating the intensification of convective process ($\boldsymbol{S_{w'}}$) and consequently the rising of the $PBLH_{MWR}$. $R_n$ begins to decrease some time before the other variables, but the intense reduction of air temperature and decrease of $\boldsymbol{S_{w'}}$ and $PBLH_{MWR}$ occurs when $R_n$ becomes negative again.

Figure 8-E presents the values of surface air temperature and surface relative humidity ($RH$). Air surface temperature is directly related with $R_n$ and $\boldsymbol{S_{w'}}$ values. On the other hand, $RH$ is inversely correlated with temperature and, thus, with the rest of variables, in fact $PBLH_{MWR}$ is higher when surface sensible heat fluxes dominate latent heat fluxes and lead to increase buoyancy, what occurs in the middle of the day.

Figure 9 shows the $RCS_{532}$ profile obtained from 08:00 to 18:00 UTC and the well-defined $PBLH_{MWR}$ (pink stars). At the beginning of the measurement period (08:20 to 10:00 UTC) it is possible to observe the presence of a thin residual layer (around 2000 m a.s.l.), and later from 13:00 to 18:00 UTC it is evident a lofted aerosol layer. Figure 10 presents the statistical moments generated from $RCS'$, which were obtained



from 13:00 and 14:00 UTC. The maximum for the variance of $RCS$ can be used as indicator of $PBLH$ ($PBLH_{Elastic}$) (Moreira et al., 2015), so the red line in all graphics represent the $PBLH_{Elastic}$ and the blue one the $PBLH_{MWR}$.

Due to well-defined $PBL$, $PBLH_{Elastic}$ and $PBLH_{MWR}$ do not have significant differences. $\boldsymbol{\sigma^2_{RCS'}}$ has small values below the $PBLH$. Above $PBLH_{Elastic}$ the values of $\boldsymbol{\sigma^2_{RCS'}}$ decrease slowly due to the location of the lofted aerosol layer around 2500 m. However, above this aerosol layer the value of $\boldsymbol{\sigma^2_{RCS'}}$ is reduced to zero, indicating the extreme decreasing in aerosol concentration in the free troposphere. The integral time scale obtained from RCS' ($\boldsymbol{\tau_{RCS'}}$) has values higher than $EL$ time acquisition throughout the CBL, evidencing the feasibility for studying turbulence using this elastic lidar configuration. The skewness values obtained from RCS' ($\boldsymbol{S_{RCS'}}$) give us information about aerosol motion. The positive values of $\boldsymbol{S_{RCS'}}$ observed in the lowest part of profile and above the $PBLH_{Elastic}$ represents the updrafts aerosol layers. The negative values of $\boldsymbol{S_{RCS'}}$ indicates the region with low aerosol concentration due to clean air coming from free troposphere ($FT$). This movement of ascension of aerosol layers and descent of clean air with zero value of $\boldsymbol{S_{RCS'}}$ is characteristic of growing PBL and was also detected by Pal et al. (2010) and McNicholas et al. (2014). The kurtosis of RCS' ($\boldsymbol{K_{RCS'}}$) determines the level of mixing at different heights. There are values of $\boldsymbol{K_{RCS'}}$ larger than 3 in the lowest part of profile and around 2500 m, showing a peaked distribution in this region. On other hand, values of $\boldsymbol{K_{RCS'}}$ lower than 3 are observed close to the $PBLH_{Elastic}$, therefore this region has a well-mixed $CBL$ regime. Pal et al. (2010) and McNicholas et al. (2014) also detected this feature in the region nearby the $PBLH$.

The results provided by $DL$, pyranometer and $MWR$ data agree with the results observed in Figure 10. In the same way, the analysis of high order moments of $RCS'$ fully agree with the information in Figure 8. Thus, the large values of $\boldsymbol{S_{RCS'}}$ and $\boldsymbol{K_{RCS'}}$ detected around 2500 m a.s.l, where we can see a lofted aerosol layer, suggest the ascent of an aerosol layer and presence of a peaked distribution, respectively.

#### 4.2.2 Case study: dusty and cloudy scenario

In this case study measurements with $DL$, $MWR$ and pyranometer expand during 24 hours, while $EL$ data are collected from 09:00 to 16:00 UTC.

Figure 11-A shows $\boldsymbol{\tau_{w'}}$, where the gray area has the same meaning mentioned earlier. Outside the period 13:00 to 17:00 UTC, the grey area is situated completely above the $PBLH_{MWR}$ (white stars), thus $DL$ time acquisition is enough to perform studies about turbulence in this case.

$\boldsymbol{\sigma^2_{w'}}$ has values close to zero during all the stable period (Figure 11-B). However, when air temperature (black lines) and $PBLH_{MWR}$ begins to increase (around 06:00 UTC), $\boldsymbol{\sigma^2_{w'}}$ also increases and reaches its maximum in the middle of the day. In the late afternoon, as air temperature and $PBLH_{MWR}$ decrease, the values of $\boldsymbol{\sigma^2_{w'}}$ decrease gradually, until reach the minimum value associated to the SBL. Figure 11-C shows the profiles of $\boldsymbol{S_{w'}}$. In the same way of the previous case study, the behavior of $\boldsymbol{S_{w'}}$ is directly related to the air temperature pattern (increasing and decreasing together) and causing the growth and reduction of $PBLH_{MWR}$. The main features of this case are: the low values of $\boldsymbol{S_{w'}}$, the slow increase and ascension of



positive $S_{w'}$ values and the predominance of negative $S_{w'}$ values from 12:00 to 13:00 UTC. The first two features are likely due to the presence of the intense Saharan dust layer (Figure 12), which reduce the passage of solar irradiance, and consequently the absorption of solar irradiance at the surface, generating weak convective process. From Figure 17 we can observe the presence of clouds from 12:00 to 14:00 UTC. This justify the intense negative values of $S_{w'}$ observed in this period, because, as mentioned before, $S_{w'}$ is directly associated with direction of turbulent movements that during this period is associated to cloud-top cooling, due to the presence of clouds (Asmann, 2010).

The influence of Saharan dust layer can also be evidenced on the $R_n$ pattern (Figure 11-D), which maintain negative values until 12:00 UTC and reach a low maximum value (around 200 W/m²). Air surface temperature and $RH$ (Figure 11-E) present the same correlation and anti-correlation (respectively) observed in the earlier case study, where the maximum of air surface temperature and the minimum of $RH$ are detected in coincidence with the maximum daily value of $PBLH_{MWR}$.

As mentioned before, Figure 12 shows the $RCS$ profile obtained from 09:00 to 16:00 UTC in a complex situation, with presence of decoupled dust layer (around 3800 m a.s.l.) from 09:00 and 12:00 and clouds (around 3500 m a.s.l.) from 11:00 to 16:00 UTC. The pink stars represent $PBLH_{MWR}$.

Figure 13 illustrates the statistical moments of $RCS'$ obtained from 11:00 to 12:00 UTC. The $\sigma^2_{RCS'}$ profile presents several peaks due to the presence of distinct aerosol sublayers. The first peak is coincident with the value of $PBLH_{MWR}$. The value of $PBLH_{elastic}$, is coincident with the base of the dust layer. This difficulty to detect the $PBLH$ in presence of several aerosol layers is inherent to the variance method (Kovalev and Eichinger, 2004). The values of $\tau_{RCS'}$ are higher than $EL$ acquisition time all along the $PBL$, evidencing the feasibility of $EL$ time acquisition for studying the turbulence of $PBL$ in this case. The $S_{RCS'}$ profile has several positive values, due to the large number of aerosol sublayers that are present. The characteristic inflection point of $S_{RCS'}$ is observed in coincidence with the $PBLH_{MWR}$, that confirming the agreement between this point and the $PBLH$. $K_{RCS'}$ has predominantly values lower than 3 below 2500 m, thus shown how this region is well mixed as can see in Figure 12. Values of $K_{RCS'}$ larger than 3 are observed in the highest part of profile, where the dust layer is located.

Figure 14 shows the $RCS'$ high-order moments obtained from 12:00 and 13:00 in presence of cloud cover. The method based on maximum of $\sigma^2_{RCS'}$ locates the $PBLH_{Elastic}$ at the cloud base, due to the high variance of $RCS'$ generated by the clouds. $\tau_{RCS'}$ presents values larger than $EL$ time acquisition, therefore this configuration enable us to study turbulence by $EL$ analyses. $S_{RCS'}$ has few peaks, due to the mixing between $CBL$ and dust layer, generating a more homogenous layer. The highest values of $S_{RCS'}$ are observed in regions where there are clouds, and the negative ones (between 3500 and 4000 m) occur due to presence of air from $FT$ between the two aerosol layers (Figure 17). The inflection point of $S_{RCS'}$ profile is observed in $PBLH_{MWR}$ region. $K_{RCS'}$ profile has low values in most of the $PBL$, demonstrating the high level of mixing during this period, where dust layer and $PBL$ are combined. The higher values of $K_{RCS'}$ are observed in the region of clouds.



## 5 Conclusions

In this paper we study the turbulence in the Planetary Boundary Layer using two different types of remote sensing systems ($DL$ and $EL$) during SLOPE-I campaign. We applied two kind of corrections to the lidar data: first lag and -2/3 corrections. The corrected $DL$ statistical moments showed little variation with respect to the uncorrected profiles, denoting a rather low influence of the noise. The statistical moments obtained from EL also showed a small variation after correction when compared with the uncorrected profiles, except for $K_{RCS}$, that is more affected by noise. The small changes in the profiles after the corrections, specially inside the $PBL$, evidence the feasibility of the applied methodology for monitoring the turbulence in the PBL. Nevertheless, all profiles are corrected by first lag correction, which is more restrictive during the comparison, in order to be cautious.

The case studies present two kind of situations: well-defined PBL and a more complex situation with the presence of Saharan dust layer and some clouds. $\sigma_w^2$, and $S_w$, showed a good agreement with the behavior of the air temperature, $R_n$ and $PBLH_{MWR}$ in both situations, highlighting the feasibility in different atmospheric conditions.

The synergic use of remote sensing systems shows how the results provided by the different instruments can complement one each other, so that, its possible to observe the direct relationship among PBL growth, $S_w$, $\sigma_w^2$, $\sigma_{RCS}^2$, and $R_n$ values. In addition, $S_{RCS}$, and $K_{RCS}$, provide a good description about aerosol dynamic. The combination of these results gives us a detailed description about PBL dynamic and its structure.

Therefore, this study shows the feasibility of the described methodology based on remote sensing systems for studying the turbulence. The feasibility of using the analyses of high order moments of the RCS collected at 532nm at a temporal resolution of 2 s for the characterization of the atmospheric turbulence in the PBL offers the possibility for using this procedure in networks like EARLINET or LALINET with a reasonable extra effort.

**Acknowledgements**

This work was supported by the Andalusia Regional Government through project P12-RNM-2409, by the Spanish Ministry of Economy and Competitiveness through project CGL2013-45410-R, CGL2016-81092-R and by the University of Granada through "Plan Propio. Programa 9 Convocatoria 2013. The financial support for EARLINET in the ACTRIS Research Infrastructure Project by the European Union's Horizon 2020 research and innovation program through project ACTRIS-2 (grant agreement No 654109). The authors thankfully acknowledge the FEDER program for the instrumentation used in this work.

## References

Alados, I., Foyo-Moreno, I., Olmo, F. J., Alados-Arboledas, L. Relationship between net radiation and solar radiation for semi-arid shrub-land. Agricultural and Forest Meteorology, 116, 221-227, 2003.

Albrecht, B. A., Bretherton, C. S., Johnson, D., Scubert, W. H., and Frisch, A. S.: The Atlantic stratocumulus transition experiment—ASTEX, Bull. Am. Meteorol. Soc., 76, 889–904, 1995.

Andrews, E., Sheridan, P. J. , Ogren, J. A., and Ferrare, R.: In situ aerosol profiles over the Southern Great Plains cloud and radiation test bed site: 1. Aerosol optical properties, J. Geophys. Res., 109, D06208, doi:10.1029/2003JD004025, 2004.

Ansmann, A., Fruntke, J., Engelmann, R. Updraft and downdraft characterization with Doppler lidar: cloud-free versus cumuli-topped mixed layer. Atmos. Chem. Phys., 10, 7845-7858, 2010.

Antón, M., Valenzuela, A., Cazorla, A., Gil, J. E., Gálvez-Fernández, J., Lyamani, H., Foyo-Moreno, I., Olmo, F. J., Alados-Arboledas, L. Global and diffuse shortwave irradiance during a strong desert dust episode at Granada (Spain). Atmospheric Research, 118, 232 – 239, 2012.

Bedoya-Velásquez, A. E., Navas-Guzmán, F., Granados-Muñoz, M. J., Titos, G., Román, R., Casquero-Vera, J. A., Ortiz-Amezcua, P., Benavent-Oltra, J. A., Moreira, G. de A., Montilla-Rosero, E., Ortiz, C. D. H., Artiñano, Coz, E., Alados-Arboledas, L., Guerrero-Rascado, J. L. Hygroscopic growth study in the framework of EARLINET during the SLOPE I campaign: synergy of remote sensing and in-situ instrumentation. Atmospheric Chemistry and Physics Discussion, doi: https://doi.org/10.5194/acp-2017-993, 2017

Behrendt, A., Wulfmeyer, V., Hammann, E., Muppa, S. K., Pal, S.: Profiles of second- to fourth-order moments of turbulent temperature fluctuations in the convective boundary layer : first measurements with rotational Raman lidar. Atmospheric Chemistry and Physics, 15, 5485–5500. https://doi.org/10.5194/acp-15-5485-2015, 2015.

Caumont, O., Cimini, D., Löhnert, U., Alados-Arboledas, L., Bleisch, R., Buffa, F., Ferrario, M.E., Haefele, A., Huet, T., Madonna, F., Pace, G. Assimilation of humidity and temperature observations retrieved from ground-based microwave radiometers into a convective-scale NWP model. Quarterly Journal of the Royal Meteorological Society, 142 (700), pp. 2692-2704, 2016.

Engelmann, R.; Wandinger, U.; Ansmann, A.; Müller, D.; Žeromskis, E.; Althausen, D.; Wehner, B. Lidar Observations of the Vertical Aerosol Flux in the Planetary Boundary Layer. Journal of Atmospheric and Oceanic Technology, v. 25, n. 8, p. 1296–1306, 2008.

Guerrero-Rascado, J.L., Ruiz, B., Alados-Arboledas, L. Multi-spectral lidar characterization of the vertical structure of Saharan dust aerosol over Southern Spain. Atmospheric Environment, 42, 2668-2681, 2008.

Guerrero-Rascado, J.L., Olmo, F.J., Avilés-Rodríguez, I., Navas-Guzmán, F., Pérez-Ramírez, D., Lyamani, H., Alados-Arboledas, L.: Extreme Saharan dust event over the southern Iberian Peninsula in September 2007: Active and passive remote sensing from surface and satellite. Atmospheric Chemistry and Physics, Volume 9, Issue 21, 8453-8469, 2009.

Guerrero-Rascado, J. L., Costa, M. J., Bortoli, D., Silva, A. M., Lyamani, H., Alados-Arboledas, L. Infrared lidar overlap function: an experimental determination, Optics Express, 18, 20350-20359, 2010



Guerrero-Rascado 2016

Kaimal, J. C., and Gaynor, J. E.: The Boulder Atmospheric Observatory, J. Clim. Appl. Meteorol., 22, 863–880, 1983.

Kiemle, C., Brewer, W. A., Ehret, G., Hardesty, R. M., Fix, A., Senff, C., Wirth, M., Poberaj, G., and LeMone, M. A.: Latent heat flux profiles from collocated airborne water vapor and wind lidars during IHOP 2002, J. Atmos. Ocean. Tech., 24, 627–639, 2007

Kovalev, V.A., Eichinger, W.E., Elastic Lidar, Wiley 2004.

Lenschow, D. H., Wyngaard, J. C., and Pennell, W. T.: Mean-field and second-moment budgets in a baroclinic convective boundary layer, J. Atmos. Sci., 37, 1313–1326, 1980.

Lenschow, D. H., Mann, J., and Kristensen, L.: How long is long enough when measuring fluxes and other turbulence statistics?, J. Atmos. Oceanic Technol., 11, 661–673, 1994.

Lenschow, D. H., Wulfmeyer, V. and Senff, C.: Measuring second- through fourth-order moments in noisy data, J. Atmos. Oceanic Technol., 17, 1330–1347, 2000.

Lenschow, D. H., Lothon, M., Mayor, S. D., Sullivan, P. P., and Canut, G.: A comparison of higher-order vertical velocity moments in the convective boundary layer from lidar with in situ measurements and large-eddy simulation, Boundary Layer Meteorol., 143, 107–123, doi:10.1007/s10546-011-9615-3., 2012.

Lothon, M., Lenschow, D. H., and Mayor, S. D.: Coherence and scale of vertical velocity in the convective boundary layer from a Doppler lidar, Bound.-Lay. Meteorol., 121, 521–536, 2006.

Lyamani, H., Olmo, F. J., Alcántara, A., and Alados-Arboledas, L.: Atmospheric aerosols during the 2003 heat wave in southeastern Spain I: Spectral optical depth, Atmos. Environ., 40, 6453–6464, 2006

McNicholas, C., Turner, D. D. Characterizing the convective boundary layer turbulence with a High Spectral Resolution Lidar. Journal of Geophysical Research: Atmospheres, v. 119, p. 910–927, 2014.

Muppa, K.S., Behrendt, A., Späth, F., Wulfmeyer, V., Metzendorf, S., Riede, A.: Turbulent humidity fluctuations in the convective boundary layer: Cases studies using water vapour differential absorption lidar measurements. Boundary-Layer Meteology, 158, 43-66, DOI 10.1007/s10546-015-0078-9, 2014.

Monin, A. S., Yaglom, A. M. Statistical Fluid Mechanics, Vol. 2. MIT Press, 874 pp, 1979.

Navas Guzmán, F., Guerrero Rascado, J. L., and Alados Arboledas, L.: Retrieval of the lidar overlap function using Raman signals, Óptica Pura y Aplicada, 44, 71–75, 2011.

Navas-Guzmán, F., Bravo-Aranda, J.A., Guerrero-Rascado, J.L, Granados-Muñoz, M.J, and Alados-Arboledas, L.: Statistical analysis of aerosol optical properties retrieved by Raman lidar over Southeastern Spain. Tellus B, 65, 21234, 2013.

Navas-Guzmán, F., Fernández-Gálvez, J., Granados-Muñoz, M.J, Guerrero-Rascado, J.L., Bravo-Aranda, J.A., and Alados-Arboledas, L.: Tropospheric water vapor and relative humidity profiles from lidar and microwave radiometry. Atmos. Meas. Tech., 7, 1201-1211, 2104.

O'Connor, E. J., Illingworth, A. J., Brooks, I. M., Westbrook, C. D., Hogan, R. J., Davies, F., Brooks, B. J.: A method for estimating the turbulent kinetic energy dissipation rate from a vertically-pointing Doppler lidar, and independent evaluation from balloon-borne in-situ measurements. Journal of Atmospheric and Oceanic Technology, v. 27, n. 10, 1652-1664, 2010.

Pal, S.; Behrendt, a.; Wulfmeyer, V. Elastic-backscatter-lidar-based characterization of the convective boundary layer and investigation of related statistics. Annales Geophysicae, v. 28, n. 3, p. 825–847, 2010.

Papalardo, G., Amodeo, A., Apituley, A., Comeron, A., Freudenthaler, V., Linné, H., Ansmann, A., Bösenberg, J., D'Amico, G., Mattis, I., Mona, L., Wandinger, U., Amiridis, V., Alados-Arboledas, L., Nicolae, D., and Wiegner, M.: EARLINET: towards an advanced sustainable European aerosol lidar network. Atmos. Meas. Tech., 7, 2389-2409, doi:10.5194/amt-7-2389-2014, 2014.

Román, R., Benavent-Oltra, J. A., Casquero-Vera, J. A., Lopatin, A., Cazorla, A., Lyamani, H., Denjean, C., Fuertes, D., Pérez-Ramirez, D., Torres, B., Toledano, C., Dubovik, O., Cachorro, V. E., Frutos, A. M., Olmo, F. J., Alados-Arboledas, L. Retrieval of aerosol profiles combining sunphotometer and ceilometer measurements in GRASP code. Atmospheric Research, 204, 161, 177, 2018.

Rose, T., Creewll, S., Löhnert, U., Simmer, C.: A network suitable microwave radiometer for operational monitoring of cloudy atmosphere. Atmospheric Research, Vol. 75, No. 3, 183 – 200, 2005.

Sicard, 2015

Stull, R. B., Santoso, E., Berg, L., Hacker, J.: Boundary layer experiment 1996 (BLX96), Bull. Am. Meteorol. Soc., 78, 1149–1158, 1997.

Stull, R. B.: An Introduction to Boundary Layer Meteorology, vol. 13, *Kluwer Academic Publishers, the Netherlands*, Dordrecht/Boston/London, 1988.

Stull, R. B.: Meteorology for Scientists and Engineers, 3rd Edition, *Uni. Of British Columbia*, 2011.

Titos, G., Foyo-Moreno, I., Lyamani, H., Querol, X., Alastuey, A., and Alados-Arboledas, L.: Optical properties and chemical composition of aerosol particles at an urban location: An estimation of the aerosol mass scattering and absorption efficiencies, J. Geophys.Res.-Atmos., 117, D04206, doi:10.1029/2011JD016671, 2012.

Turner, D. D., Ferrare, R. A., Wulfmeyer, V., and Scarino, A. J.: Aircraft evaluation of ground-based Raman lidar water vapor turbulence profiles in convective mixed layers, J. Atmos. Oceanic Technol., 31, 1078–1088, doi:10.1175/JTECH-D-13-00075-1, 2014

van Ulden, A. P., and Wieringa, J. :Atmospheric boundary layer research at Cabauw, Boundary-Layer Meteorol., 78,39–69, 1996.

Valenzuela, A., Olmo, F.J.ab, Lyamani, H.ab, Granados-Muñoz, M.J.ab, Antón, M.c, Guerrero-Rascado, J.L.ab, Quirantes, A.a, Toledano, C.d, Perez-Ramírez, D.ef, Alados-Arboledas, L.: Aerosol transport over

the western mediterranean basin: Evidence of the contribution of fine particles to desert dust plumes over alborán island. Journal of Geophysical Research Volume 119, Issue 24, 14,028-14,044, 2014.

Vogelmann, A. M., McFarquhar, G. M., Ogren, J. A., Turner, D. D., Comstock, J. M., Feingold, G., Long, C. N., Jonsson, H. H., Bucholtz, A., Collins, D. R., Diskin, G. S., Gerber, H., Lawson, R. P., Woods, R. K., Andrews, E., Yang, H., Chiu, J. C., Hartsock, D., Hubbe, J. M., Lo, C., Marshak, A., Monroe, J. W., Mcfarlane, S. A., Jason, M., and Toto, T.: RACORO extended-term aircraft observations of boundary layer clouds, Bull. Am. Meteorol. Soc., 93, 861–878, doi:10.1175/BAMS-D-11-00189.1, 2012.

Williams, A. G., and Hacker, J. M.: The composite shape and structure of coherent eddies in the convective boundary layer, Boundary Layer Meteorol., 61, 213–245, 1992.

Wulfmeyer, V.: Investigation of turbulent processes in the lower troposphere with water vapor DIAL and radar-RASS, J. Appl. Sci., 56, 1055–1076, 1999.

Wulfmeyer, V., Pal., S., Turner, D. D., and Wagner, E.: Can water vapour Raman lidar resolve profiles of turbulent variables in the convective boundary layer?, Boundary Layer Meteorol., 136, 253–284, doi:10.1007/s10546-010-9494-z, 2010.

Atmos. Chem. Phys. Discuss., https://doi.org/10.5194/acp-2018-276
Manuscript under review for journal Atmos. Chem. Phys.
Discussion started: 16 April 2018


Atmospheric Chemistry and Physics Discussions

Table 1 – Variables applied to statistical analysis (Lenschow et al., 2000)

| | Without Correction | Correction | Error |
|---|---|---|---|
| **Integral Time Scale ($\tau$)** | $\int_0^{\infty} q'(t)dt$ | $\frac{1}{\overline{q'^2}} \int_{t\to 0}^{\infty} M_{11}(t)dt$ | $\tau . \sqrt{\frac{4\Delta M_{11}}{M_{11}(\to 0)}}$ |
| **Variance ($\sigma^2_{q'}$)** | $\frac{1}{T}\sum_{t=1}^{T}(q(t) - \overline{q})^2$ | $M_{11}(\to 0)$ | $q^2 . \sqrt{\frac{4\Delta M_{11}}{M_{11}(\to 0)}}$ |
| **Skewness ($S$)** | $\frac{\overline{q^3}}{\sigma_q^3}$ | $\frac{M_{21}(\to 0)}{M_{11}^{3/2}(\to 0)}$ | $\frac{\Delta M_{21}}{\Delta M_{11}^{3/2}}$ |
| **Kurtosis ($K$)** | $\frac{\overline{q^4}}{\sigma_q^4}$ | $\frac{3M_{22}(\to 0) - 2M_{31}(\to 0) - 3\Delta M_{11}^2}{M_{11}^2(\to 0)}$ | $\frac{4\Delta M_{31} - 3\Delta M_{22} - \Delta M_{11}^2}{\Delta M_{11}^2}$ |

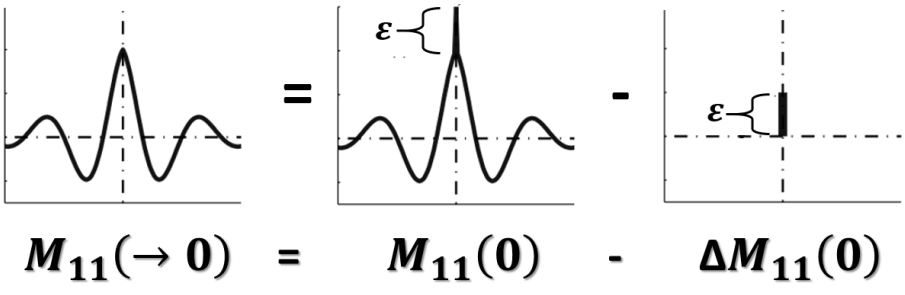


Figure 1 – Procedure to remove the errors of autocovariance functions. $M_{11}(\to 0)$ – corrected autocovariance function errors; $M_{11}(0)$ - autocovariance function without correction; $\Delta M_{11}(0)$ - error of autocovariance function

Atmos. Chem. Phys. Discuss., https://doi.org/10.5194/acp-2018-276
Manuscript under review for journal Atmos. Chem. Phys.
Discussion started: 16 April 2018


Atmospheric Chemistry and Physics Discussions

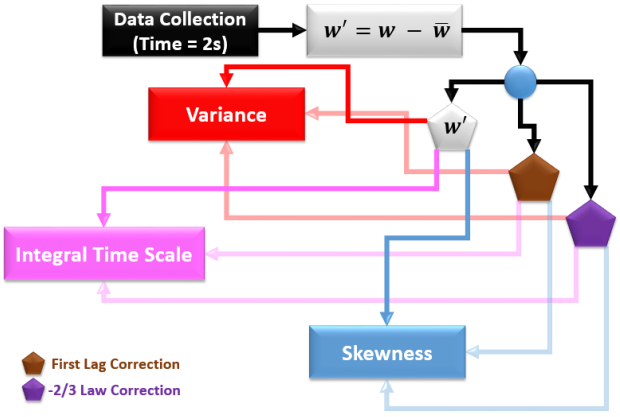


Figure 2 – Flowchart of data analysis methodology applied to the study of turbulence with Doppler lidar

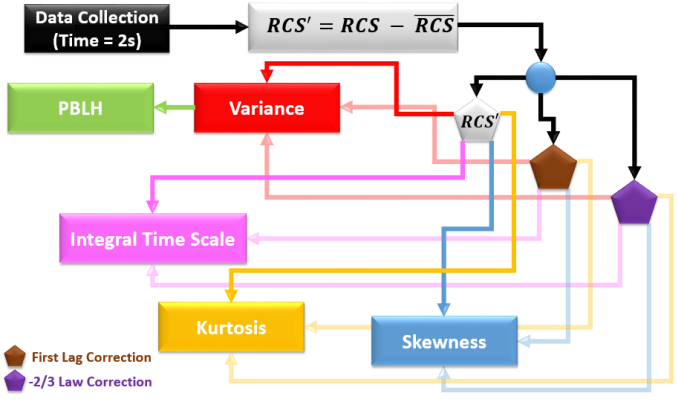


Figure 3 – Flowchart of data analysis methodology applied to the study of turbulence with elastic lidar

Atmos. Chem. Phys. Discuss., https://doi.org/10.5194/acp-2018-276
Manuscript under review for journal Atmos. Chem. Phys.
Discussion started: 16 April 2018


Atmospheric Chemistry and Physics Discussions

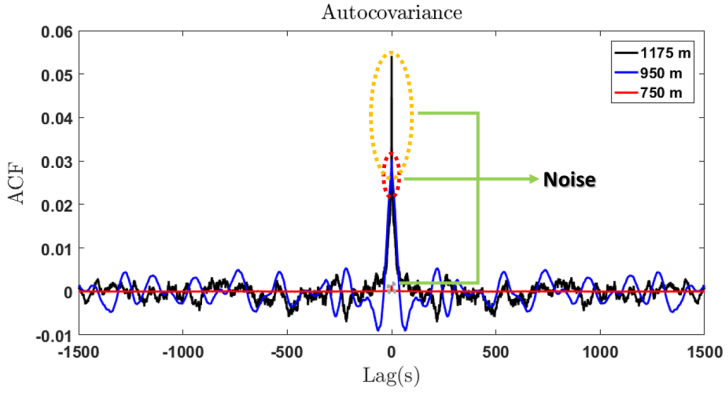


Figure 4 – Autocovariance function (ACF) of w' at three different heights

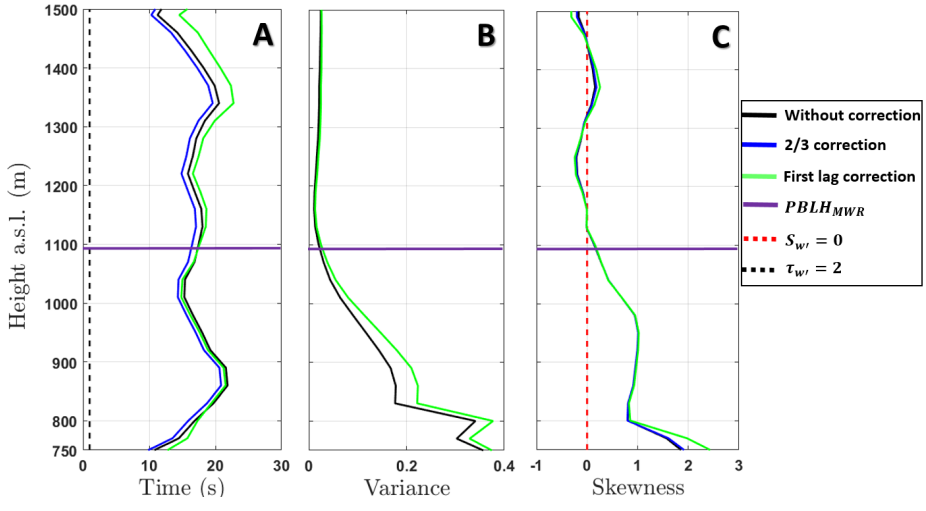


Figure 5 – A - Vertical profile of Integral time scale ($\tau_{w'}$). B - Vertical profile of variance ($\sigma^2_{w'}$). C - Vertical profile of Skewness. ($S_{w'}$)

Atmos. Chem. Phys. Discuss., https://doi.org/10.5194/acp-2018-276
Manuscript under review for journal Atmos. Chem. Phys.
Discussion started: 16 April 2018


Atmospheric Chemistry and Physics Discussions

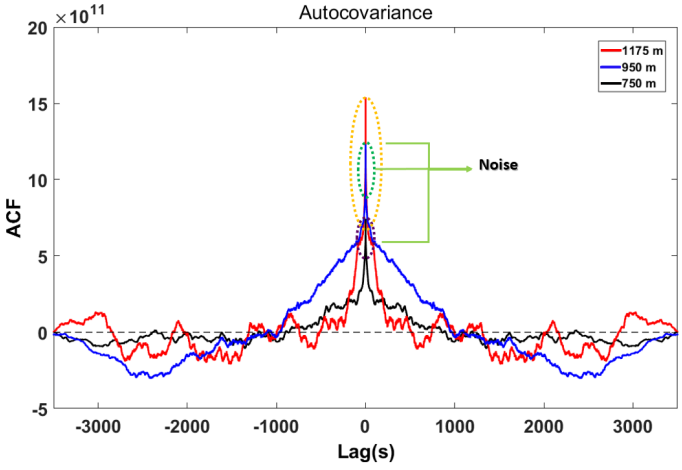


Figure 6 – Autocovariance of RCS' to three different heights

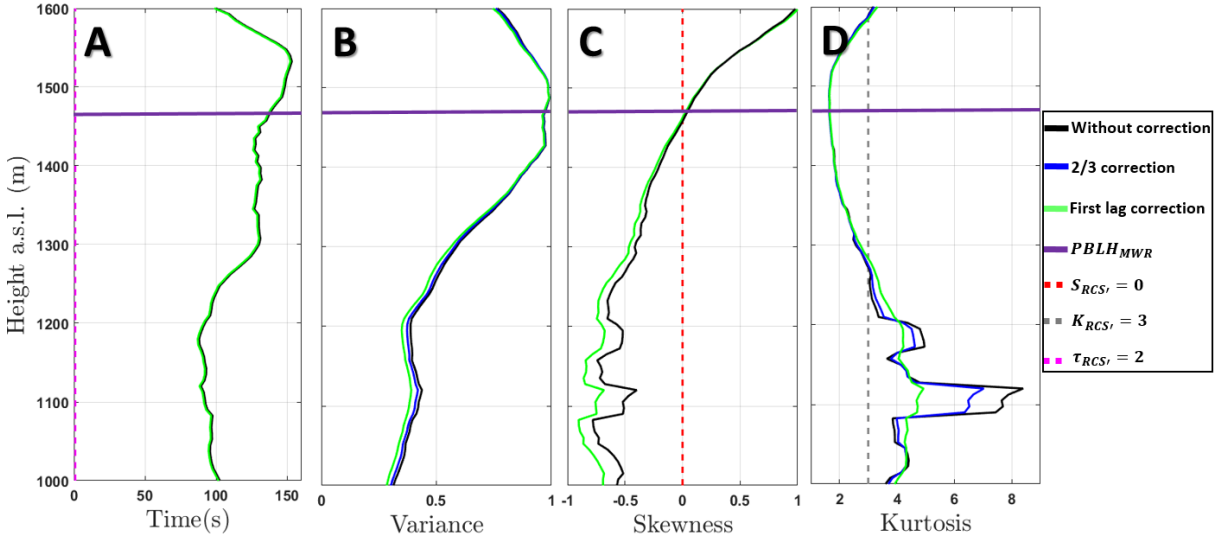


Figure 7 – A- Vertical profile of Integral time scale ($\boldsymbol{\tau_{RCS'}}$). B - Vertical profile of variance ($\boldsymbol{\sigma^2_{RCS'}}$). C - Vertical profile of Skewness ($\boldsymbol{S_{RCS'}}$). D - Vertical profile of Kurtosis ($\boldsymbol{K_{RCS'}}$).

Atmos. Chem. Phys. Discuss., https://doi.org/10.5194/acp-2018-276
Manuscript under review for journal Atmos. Chem. Phys.
Discussion started: 16 April 2018


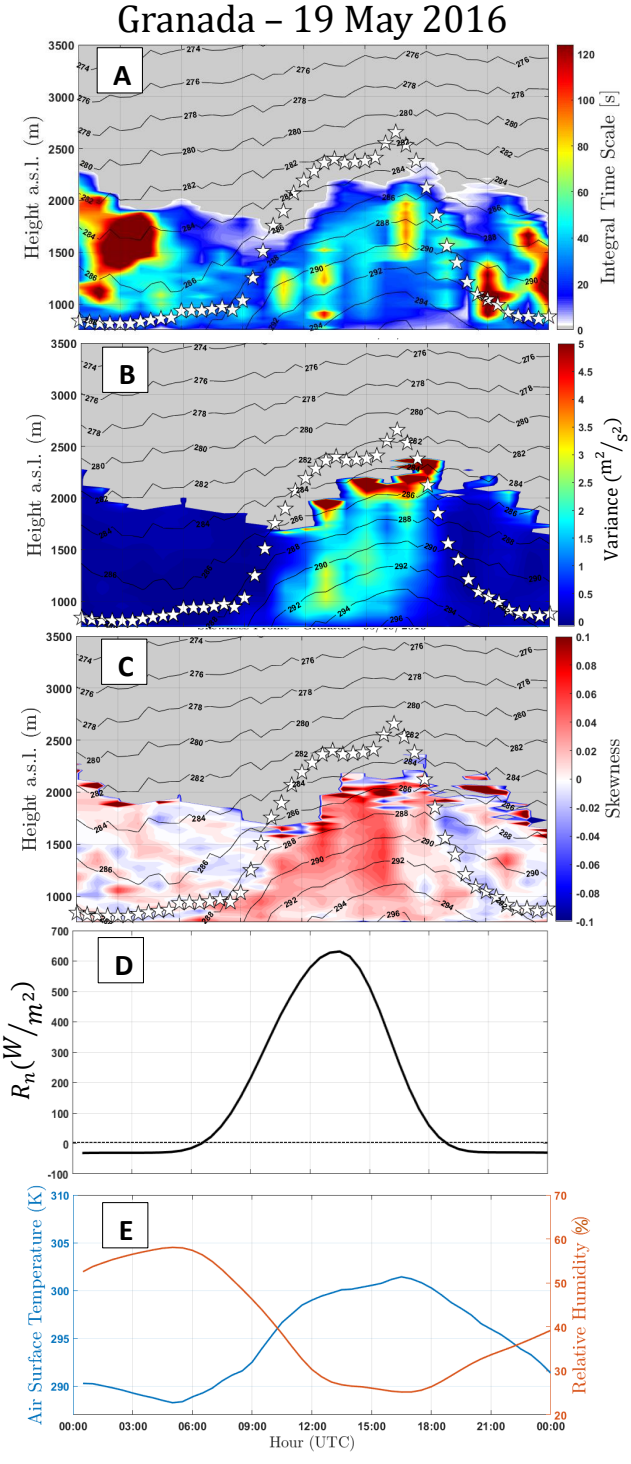


Figure 8 – A – integral time scale [$\boldsymbol{\tau_{w'}}$], B – variance [$\boldsymbol{\sigma^2_{w'}}$], C – skewness [$\boldsymbol{S_{w'}}$], D – net radiation [$R_n$], E – Air surface temperature [blue line] and surface relative humidity [$RH$ – orange line]. In A, B and C black lines and white stars represent air temperature and $PBLH_{MWR}$, respectively.

Atmos. Chem. Phys. Discuss., https://doi.org/10.5194/acp-2018-276
Manuscript under review for journal Atmos. Chem. Phys.
Discussion started: 16 April 2018


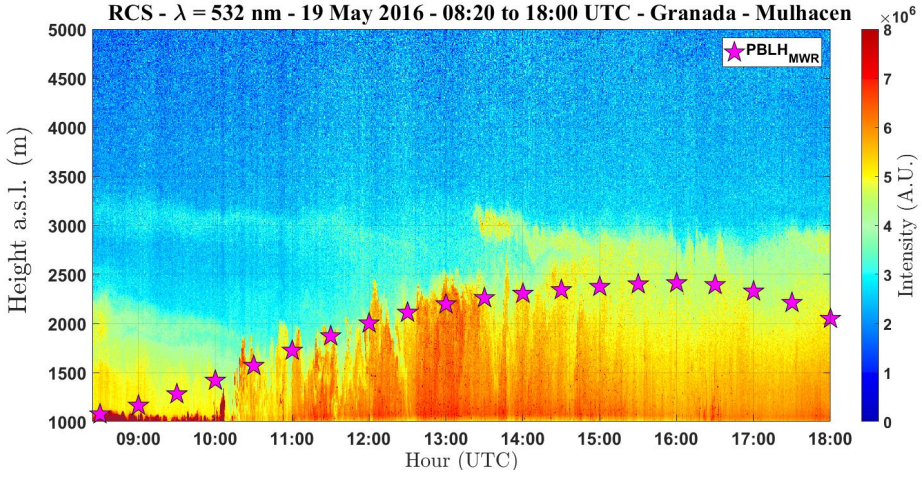


Figure 9 – RCS Profile 19 May 2016. Pink stars represent $PBLH_{MWR}$

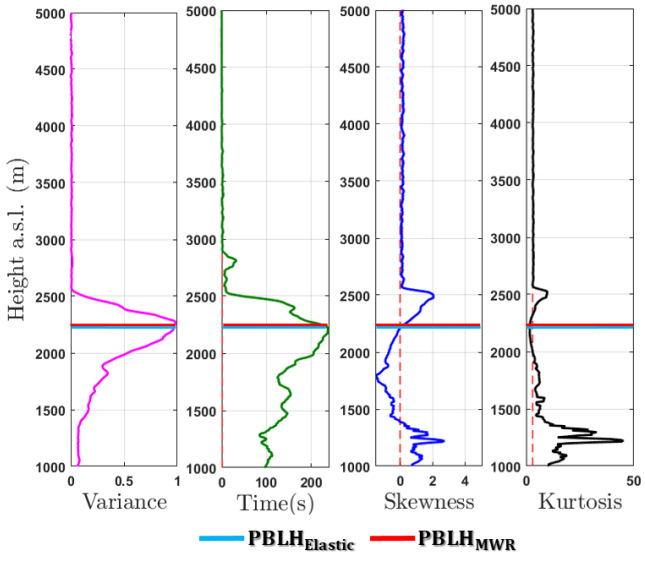


Figure 10 – Statistical moments obtained from elastic lidar data at 13 to 14 UTC - 19 May 2016. From left to right: variance [$\boldsymbol{\sigma^2_{RCS'}}$], integral time scale [$\boldsymbol{\tau_{RCS'}}$], skewness [$\boldsymbol{S_{RCS'}}$] and kurtosis [$\boldsymbol{K_{RCS'}}$].

Atmos. Chem. Phys. Discuss., https://doi.org/10.5194/acp-2018-276
Manuscript under review for journal Atmos. Chem. Phys.
Discussion started: 16 April 2018


Atmospheric Chemistry and Physics Discussions

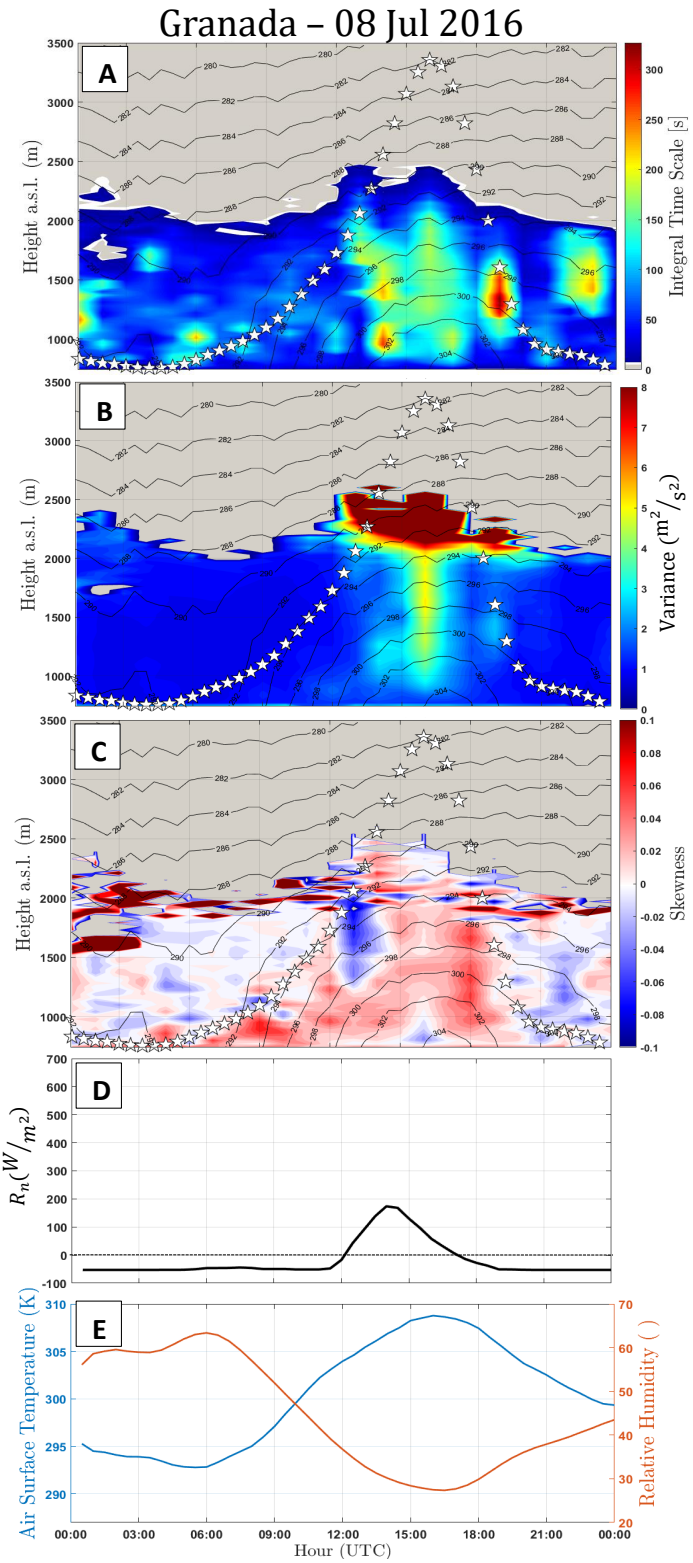


Figure 11 - A – integral time scale [$\boldsymbol{\tau_{w'}}$], B – variance [$\boldsymbol{\sigma^2_{w'}}$], C – skewness [$\boldsymbol{S_{w'}}$], D – net radiation [$R_n$], E – Air surface temperature [blue line] and surface relative humidity [$RH$ – orange line]. In A, B and C black lines and white stars represent air temperature and $PBLH_{MWR}$, respectively.

Atmos. Chem. Phys. Discuss., https://doi.org/10.5194/acp-2018-276
Manuscript under review for journal Atmos. Chem. Phys.
Discussion started: 16 April 2018


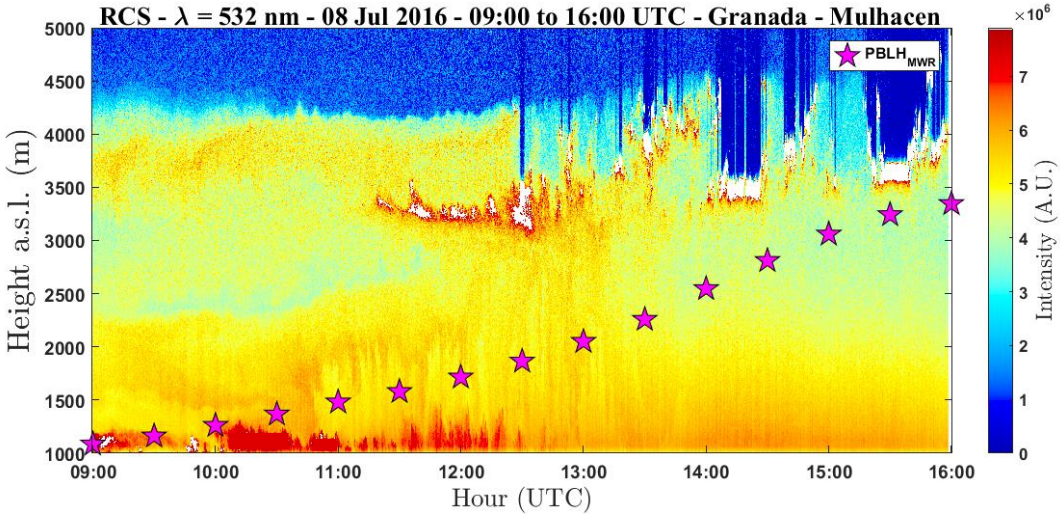


Figure 12 - RCS Profile 08 July 2016. Pink stars represent $PBLH_{MWR}$.

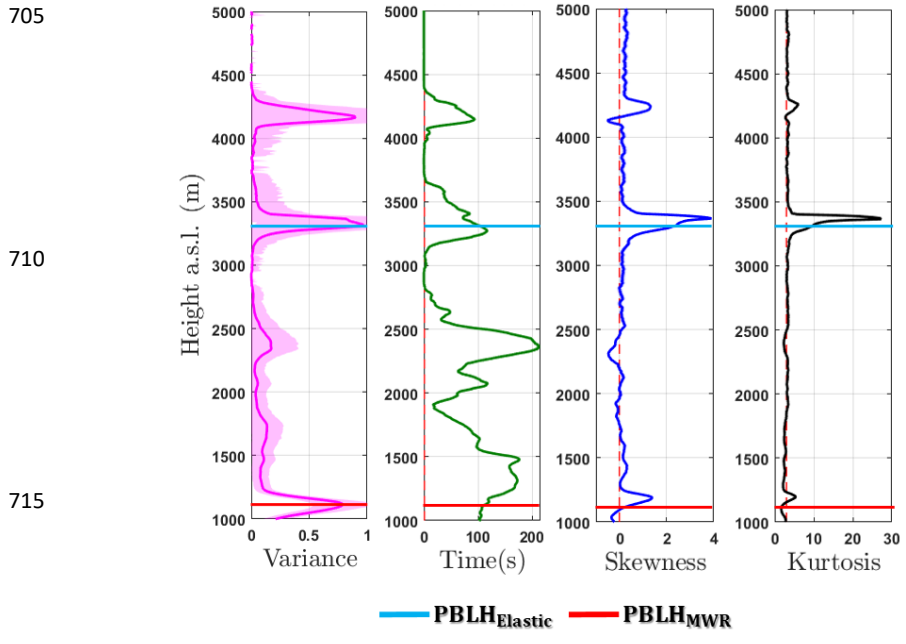


Figure 13 - Statistical moments obtained from elastic lidar data at 11 to 12 UTC - 08 July 2016. From left to right: variance [$\sigma^2_{RCS'}$], integral time scale [$\tau_{RCS'}$], skewness [$S_{RCS'}$] and kurtosis [$K_{RCS'}$].

Atmos. Chem. Phys. Discuss., https://doi.org/10.5194/acp-2018-276
Manuscript under review for journal Atmos. Chem. Phys.
Discussion started: 16 April 2018


Atmospheric Chemistry and Physics Discussions

720

725

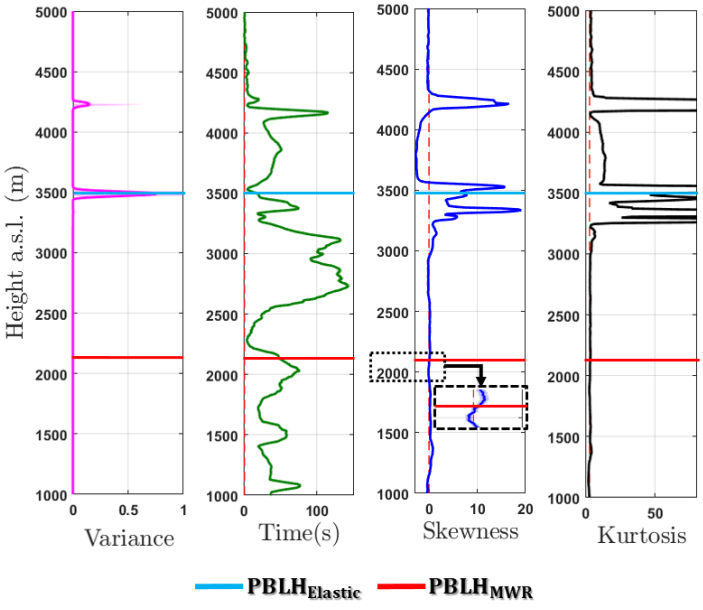


Figure 14 - Statistical moments obtained from elastic lidar data at 12 to 13 UTC - 08 July 2016. From left to right: variance [$\sigma^2_{RCS'}$], integral time scale [$\tau_{RCS'}$], skewness [$S_{RCS'}$] and kurtosis [$K_{RCS'}$].